OXFORD

High cortical iron is associated with the disruption of white matter tracts supporting cognitive function in healthy older adults

Valentinos Zachariou (ID) [1,2,*], Christopher E. Bauer[1,2], Colleen Pappas[1,2], Brian T. Gold[1,2,3,4,*]

[1]Department of Neuroscience, University of Kentucky, Lexington, KY 40536-0298, United States,
[2]College of Medicine, University of Kentucky, Lexington, KY 40536-0298, United States,
[3]Sanders-Brown Center on Aging, University of Kentucky, Lexington, KY 40536-0298, United States,
[4]Magnetic Resonance Imaging and Spectroscopy Center, University of Kentucky, Lexington, KY 40536-0298, United States

*Corresponding author: Department of Neuroscience, University of Kentucky College of Medicine, MN 364 Medical Sciences Building, 780 Rose Street, Lexington, KY 40536-0298, USA. Email: vzachari@uky.edu (Valentinos Zachariou); brian.gold@uky.edu (B. T. Gold)

Aging is associated with brain iron accumulation, which has been linked to cognitive decline. However, how brain iron affects the structure and function of cognitive brain networks remains unclear. Here, we explored the possibility that iron load in gray matter is associated with disruption of white matter (WM) microstructure within a network supporting cognitive function, in a cohort of 95 cognitively normal older adults (age range: 60–86). Functional magnetic resonance imaging was used to localize a set of brain regions involved in working memory and diffusion tensor imaging based probabilistic tractography was used to identify a network of WM tracts connecting the functionally defined regions. Brain iron concentration within these regions was evaluated using quantitative susceptibility mapping and microstructural properties were assessed within the identified tracts using neurite orientation dispersion and density imaging. Results indicated that high brain iron concentration was associated with low neurite density (ND) within the task-relevant WM network. Further, regional associations were observed such that brain iron in cortical regions was linked with lower ND in neighboring but not distant WM tracts. Our results provide novel evidence suggesting that age-related increases in brain iron concentration are associated with the disruption of WM tracts supporting cognitive function in normal aging.

Key words: quantitative susceptibility mapping; aging; brain iron; demyelination; oxidative stress.

Introduction

Non-heme brain iron is essential for neuronal function and is involved in multiple cellular processes, such as adenosine triphosphate (ATP) generation in mitochondria, neurotransmitter synthesis, and myelin generation. However, non-heme iron is also a potent oxidizer (Todorich et al. 2009; Mills et al. 2010; Ward et al. 2014; Raz and Daugherty 2018) that contributes to the endogenous production of reactive oxygen species (ROS; Chakravarti and Chakravarti 2007). ROS can react with cellular structures (e.g. lipids, proteins, and nucleic acids), interfering with normal cell processes and damaging neurons, glia, and myelin (Wayne Martin et al. 1998; Zecca, Youdim, et al. 2004; Chakravarti and Chakravarti 2007; Ke and Qian 2007; Daugherty et al. 2015; Daugherty and Raz 2016; Raz and Daugherty 2018; Butterfield and Halliwell 2019). As a result, in healthy brain cells, non-heme brain iron is typically sequestered in intracellular iron storage complexes like ferritin and is released in a tightly regulated manner (Hentze et al. 2004; Moos et al. 2007).

However, normal aging perturbs the iron sequestration process, allowing non-heme iron to accumulate outside of storage complexes, which increases oxidative stress (Lauffer 1992; Wayne Martin et al. 1998; Zecca, Stroppolo, et al. 2004, Zecca, Youdim, et al. 2004). Age-related accumulation of non-heme brain iron

has been associated with lower cognitive and motor performance, including on measures of general cognitive ability, working memory, and episodic memory (Sullivan et al. 2009; Kim et al. 2017; Acosta-Cabronero et al. 2018; van Bergen et al. 2018; Zachariou et al. 2020). Recently, several studies have also reported a negative relationship between brain iron load and functional connectivity of cognitive brain networks in older adults (Salami et al. 2018; Rodrigue et al. 2020; Zachariou et al. 2020).

In contrast, the relationship between brain iron load and white matter (WM) connectivity, which provides the scaffolding for functional connectivity, has been relatively under-explored. Age-related increases in non-heme brain iron could disrupt WM tracts connecting cognitive networks given that increased unbound iron can contribute to demyelination via several biological mechanisms, including altered ion channel activity (Stys 2005; Lassmann and van Horssen 2016), mitochondrial dysfunction (Smith et al. 1999; Lassmann and van Horssen 2016; Raz and Daugherty 2018), and free radical damage affecting oligodendrocytes and myelin (Graham et al. 1993; Todorich et al. 2009; Bartzokis et al. 2011).

It is not currently possible to measure iron load in WM using magnetic resonance imaging (MRI) due to the diamagnetic effect of myelin on susceptibility relative to other brain compartments such as gray matter (GM) and cerebrospinal fluid (CSF).

Consequently, existing studies have focused on associations between GM iron and WM microstructure assessed with diffusion tensor imaging (DTI). To date, few studies have explored these associations and this research has generally been limited to studies of patients with multiple sclerosis (MS), a progressive neurodegenerative disease involving demyelination and increased iron load (e.g. Raz et al. 2015; Zivadinov et al. 2018) or patients with cerebral autosomal dominant arteriopathy with subcortical infarcts and leukoencephalopathy (CADISIL), a small vessel disease characterized by widespread WM tract injury (Jokinen et al. 2013; Hong et al. 2022).

One study in MS patients reported no relationship between brain iron assessed with magnetic field correlation (MFC) values and WM DTI metrics (Raz et al. 2015). In contrast, another study found a relationship between brain iron load assessed with MRI phase values in deep GM regions and multiple DTI metrics in a number of WM tracts in MS patients (Bergsland et al. 2017). Within healthy controls, this study reported only a single correlation between MRI phase values in the left caudate and FA. Recently, an additional study focused on CADASIL reported higher iron load within deep GM regions of the patients compared to the control group. Within these deep GM regions, CADASIL patients showed a negative association between iron load and DTI-based metrics in WM tracts. In contrast, no associations were observed in the healthy control group (Hong et al. 2022).

Thus, at present, little remains known about the relationship between brain iron load, WM microstructure and cognition in healthy older adults. This may be in part because previous studies have restricted their analyses to regions showing higher iron load, or lower WM integrity, in patient compared to control groups rather than focusing on brain networks supporting specific cognitive tasks. Previous null effects could also relate to the relatively young ages of healthy control groups (Raz et al. 2015: mean age 36 years; Bergsland et al. 2017: 45.5 years; Hong et al. 2022: 55.7 years). In the current study, we evaluate associations between brain iron concentration and WM microstructure in a network of tracts supporting cognitive performance in healthy older adults (mean age: 69.7 years). The cognitive domain of working memory was selected due to the well-documented, negative relationship between brain iron concentration and working memory performance in older adults (Bartzokis et al. 2011; Daugherty et al. 2015; Darki et al. 2016; Zachariou et al. 2020, 2021).

Brain iron load was assessed using quantitative susceptibility mapping (QSM), a validated methodology for evaluating brain iron concentrations (Langkammer et al. 2012; Liu, Surapaneni, et al. 2012; Sun et al. 2015; Hametner et al. 2018). Specifically, brain iron concentrations were assessed within working memory cortical regions identified using a functional MRI (fMRI)-based visual working memory task. Neurite orientation dispersion and density imaging (NODDI) was used to assess WM microstructure health within tracts interconnecting the fMRI-defined working memory regions, delineated using DTI-based probabilistic tractography. NODDI was used here because it is a more sensitive method (By et al. 2017; Schneider et al. 2017) and more closely linked to biology than more traditional DTI-based metrics. For example, several in-vitro histological studies have linked NODDI-based neurite density (ND), a voxel-wise estimate of the density of dendrites and axons, with neurite degradation and demyelination (Jespersen et al. 2010; Sepehrband et al. 2015; Wang et al. 2019). Given the link between unbound iron and both demyelination and neurite degradation (Graham et al. 1993; Smith et al. 1999; Todorich et al. 2009; Bartzokis et al. 2011; Raz and Daugherty 2018), we hypothesized that QSM-based iron concentration would

Table 1. Group demographics and mean cognitive measures.

n	95
M:F	35:60
Age range (years)	60–86
Age (years)	69.7±5.7[a]
Education (years)	16.51±2.48[a]
MoCA[b]	27.12±2.26[a]

[a]Mean ± standard deviation is shown for participants. [b]MoCA: Montreal Cognitive Assessment.

be negatively correlated with ND in a network of tracts supporting working memory performance.

Materials and methods
Participants

Ninety-eight healthy older adults were recruited for the experiment from an existing longitudinal cohort at the Sanders-Brown Center on Aging (Schmitt et al. 2013) and the broader Lexington, KY, community. All participants provided informed consent under a protocol approved by the Institutional Review Board of the University of Kentucky. All participants were cognitively intact based on either 1) clinical consensus diagnosis and scores from the Uniform Data Set (UDS3) used by US ADCs (procedure outlined in Morris et al. 2006; Besser et al. 2018) or 2) a score of 26 or higher on the Montreal Cognitive Assessment (MoCA; Nasreddine and Phillips 2005) for those participants recruited from the community.

Study exclusionary criteria were self-reported significant head injury (defined as loss of consciousness for more than 5 min), heart disease, neurological or psychiatric disorders, claustrophobia, pacemakers, the presence of metal fragments or any metal implants that are incompatible with MRI, diseases affecting the blood (anemia, kidney/heart disease etc.) or significant brain abnormalities detected during imaging.

Two participants were excluded from analyses on the basis of MRI abnormalities. One participant was excluded due to the presence of an old stroke that was not clinically evident at study enrollment and another due to being diagnosed with hydrocephalus based on MRI scans collected during the study. Additionally, 1 participant was excluded due to excessive motion during the QSM scan, resulting in a final sample size of 95 participants. Characteristics of the participant cohort are shown in Table 1. Fifty-five of the subjects in the current study also participated in Zachariou et al. (2020), while 73 subjects also participated in Zachariou et al. (2021).

Imaging protocol

Participants were scanned with a Siemens 3 T Prisma scanner (software version MR_VE11C), using a 64-channel head-coil, at the University of Kentucky Magnetic Resonance Imaging and Spectroscopy Center (MRISC). The following sequences were used: 1) a 3D multi-echo, T1-weighted, magnetization prepared rapid gradient echo sequence (MEMPR); 2) an fMRI, T2*-weighted, gradient-echo, echo-planar imaging (EPI) sequence comprised of 2 runs (4.07 min each); 3) a double-echo gradient-echo field map sequence for spatial distortion correction of the fMRI data; 4) a 3D, multi-echo, gradient-recalled echo (GRE) sequence used for quantitative susceptibility mapping (QSM); 5) a multi-shell, spin-echo, echo-planar diffusion weighted imaging (DWI) sequence (main DWI scan); and 6) a second spin-echo, echo-planar DWI sequence with the phase-encoding direction reversed, used to correct susceptibility-induced distortions in the main DWI scan.

Several other sequences were collected during the scanning session related to other scientific questions and are not discussed further here.

The MEMPR sequence had 4 echoes [repetition time (TR) = 2,530 ms; first echo time (TE1) = 1.69 ms echo time spacing (ΔTE) = 1.86 ms, flip angle (FA) = 7°] and covered the entire brain [176 slices, field of view = 256 mm, parallel imaging (GRAPPA), acceleration factor = 2, 1 mm isotropic voxels, scan duration = 5.53 min]. A MEMPR sequence was used to optimize the FreeSurfer cortical segmentation and accuracy of gray matter (GM) masks (van der Kouwe et al. 2008). The 2 fMRI runs used an EPI sequence with the following parameters: TR = 2,500 ms, TE = 30 ms, flip angle = 90°, resolution = 3.0 mm isotropic voxels, 64 × 64 matrix, field of view = 192 mm, 40 axial slices covering the whole brain. The GRE field map scan was acquired right after the second EPI sequence at the same resolution, field of view and number of axial slices as the EPI sequences. The sequence used for QSM was a flow compensated, multi-echo, 3D spoiled GRE sequence in the sagittal plane with 8 echoes (TR/TE1/ΔTE/FA = 24 ms/2.98 ms/2.53 ms/15°). The entire brain was covered [acquisition matrix = 224 × 224 × 144, parallel imaging (GRAPPA), acceleration = 2, 1.2 mm isotropic voxels and scan duration = 6.18 min]. The main DWI scan was acquired with 126 separate diffusion directions [232 x 232 x 162 mm acquisition matrix (81 slices), 2 mm isotropic voxels, TR = 3,400 ms, TE = 71 ms, scan duration = 7.45 min, posterior-to-anterior phase encoding direction] and 4 b-values (0, 500, 1,000, and 2,000 s/mm^2). The short (28 s) reverse-phase encoding direction (anterior-to-posterior) DWI scan was acquired immediately following the main DWI scan. This reverse-phase DWI scan had the same scan parameters as the main DWI scan but only 4 volumes were collected at a b-value of 0 s/mm^2.

fMRI task design

The visual working memory task is described in detail in our previous work (Zachariou et al. 2020). Briefly, participants performed an N-Back visual working memory paradigm with 3 conditions (compare, 1-Back and 2-Back) in a blocked design. During the task, participants decided if the stimulus presented in the current trial (a consonant letter) matched the stimulus in the directly preceding trial for the 1-Back condition or 2 trials back for the 2-Back condition. Responses ("same" or "different") were made using MRI compatible button-boxes (1 in each hand). The 1-Back and 2-Back conditions were contrasted to a control (compare) condition in which participants decided if 2 stimuli presented simultaneously on the screen matched.

Behavioral data analyses

Behavioral data collected during the scans were imported to Excel in order to calculate D-prime (Stanislaw and Todorov 1999) for each of the N-Back task conditions. D-prime is a measure of discrimination performance corrected for response bias. That is, the participants' tendency to respond with either "same" or "different" in a trial of the N-back task when they are uncertain or guessing. For this reason, D-prime is a more optimal measure of task performance in forced-choice discrimination tasks than accuracy that does not account for response bias. N-back task performance was ultimately expressed as the log of D-prime, averaged across the 1-Back and 2-Back conditions. Log D-prime was used in subsequent analyses involving MRI-based measures as done in our previous work (Zachariou et al. 2020, 2021), and under the assumption that large differences in D-prime are typically associated with smaller differences in MRI-based measures.

fMRI pre-processing

Functional scans were first corrected for field inhomogeneity induced geometric distortions using FUGUE and the GRE field map data in FSL (Smith et al. 2004; Jenkinson et al. 2012). Subsequently the functional scans were motion corrected and/or de-spiked where necessary (https://afni.nimh.nih.gov/pub/dist/doc/program_help/3dDespike.html) and co-registered to their contrast-corrected (using Siemens Prescan Normalize) anatomical image, after averaging the 4 echoes of a MEMPR scan into a single root mean square image and stripping the skull using FreeSurfer 6.0 (Dale et al. 1999; Desikan et al. 2006; van der Kouwe et al. 2008). Following registration, the functional scans were warped to MNI space, using the MNI ICBM152, 1 mm, 6th generation atlas (Grabner et al. 2006; referred to as MNI152 hence forth for brevity) and a non-linear transformation (3dQwarp), smoothed with a Gaussian kernel of 6.0 mm FWHM and mean-based intensity normalized (all volumes by the same factor) using AFNI (Cox 1996). In addition, linear and non-linear trends (where necessary) were removed during pre-processing of the data and motion parameters were regressed separately for each run from all analyses. Lastly, all TR pairs in which the Euclidean Norm of the motion derivative exceeded 0.3 (the AFNI default for adults) were censored and removed from the analyses.

fMRI analyses

Group-level, whole brain contrasts between N-back conditions were performed to localize a set of cortical brain regions supporting working memory performance. The group level analysis of the N-Back task was conducted using the Analysis of Functional NeuroImages software (AFNI; Cox 1996) and a linear mixed effects model (3dLME; Chen et al. 2013) with participant age added as a covariate. The functional contrast of 2-Back/2 + 1-Back/2 > Compare was used to identify brain regions in which activity for the N-Back task was greater than that of the visual control task (compare condition). The resulting statistical maps were adjusted for multiple comparisons using the false discovery rate (FDR) approach (Genovese et al. 2002). A very conservative threshold of qFDR < 2 x 10^{-13} was used to limit brain activity to the most statistically significant voxels, aiding in the delineation of distinct peaks of activity. Twelve peaks of activity were identified using this method (see Results, *fMRI N-Back Activation*) on which 8 mm diameter spheres were centered and acted as fMRI seed regions of interest (ROIs) in a subsequent probabilistic tractography analysis.

DWI pre-processing

Each participant's main DWI scan was first corrected for susceptibility induced field distortions using the corresponding reverse-phase encoding direction (anterior-to-posterior), DWI scan in FSL's topup (Andersson et al. 2003). Subsequently, DWI scans were skull-stripped using BET (Smith 2002), and non-linearly corrected for eddy currents and participant head motion using eddy (Andersson and Sotiropoulos 2016). Specifically, the Compute Unified Device Architecture (CUDA) version of eddy was used (eddy_cuda9.1), to significantly increase processing speed. The eddy corrected DWI scans were then examined visually for quality and the average head motion across volumes for each participant was assessed using the eddy QC tools (average voxel displacement across all voxels within a brain mask relative to the first volume; Bastiani et al. 2019). Average voxel displacement did not exceed 2 mm (the size of 1 DWI scan voxel) and, as such, no participants were excluded during this QC process.

Neurite orientation dispersion and density imaging processing

The eddy corrected DWI scans for each participant obtained in the previous section were used as inputs to the NODDI toolbox (version 1.04; Zhang et al. 2012) in MATLAB (version R2019 Update 7), executed with default/recommended parameters to generate intracellular volume fraction (ICVF), isotropic volume fraction (V_{iso}) and orientation dispersion index (ODI) maps. Specifically, NODDI models 3 diffusion compartments: 1) an intra-neurite compartment comprised of hindered anisotropic diffusion, corresponding to intra axonal/dendritic space; 2) an extra-neurite compartment comprised of restricted anisotropic diffusion that corresponds to the space around neurites, including neuronal and glial cell bodies; and 3) a free water compartment comprised of unrestricted, isotropic diffusion corresponding to CSF (Zhang et al. 2012).

ICVF, or ND, is calculated by dividing the intra-neurite compartment by the sum of the intra-neurite and extra-neurite compartments and represents a voxel-wise estimate of the density of dendrites and axons. V_{iso} is calculated by dividing the free water compartment by the sum of all 3 compartments (intra-neurite + extra-neurite + free water compartment) and represents a voxel-wise estimate of isotropically diffusing water; that is, the portion/fraction of each voxel that overlaps with CSF. Lastly, ODI is calculated from the orientation distribution function of the *sticks* (cylinders of radius 0) used to model water diffusion in the intra-cellular compartment, constrained to a Watson distribution (Zhang et al. 2012). In short, ODI represents a voxel-wise estimate of the degree of fiber coherence (from completely aligned straight fibers to completely isotropic fibers). Following the generation of the ND, V_{iso} and ODI maps, the V_{iso} maps were used to suppress any remaining CSF signal within the ND and ODI maps, as recommended in Zhang et al. 2012. Specifically, all voxels within an ND or ODI map with V_{iso} values greater than the 80th percentile of values in the corresponding V_{iso} map were set to zero.

A focus on neurite density

ND has been associated in previous histological studies with neurite degradation and demyelination (e.g. Sepehrband et al. 2015; Wang et al. 2019; Rahmanzadeh et al. 2021). Consequently, consistent with the contribution of unbound iron to demyelination (Graham et al. 1993; Smith et al. 1999; Todorich et al. 2009; Bartzokis et al. 2011; Raz and Daugherty 2018), we focused our analyses on ND as the main measure of WM microstructure health.

In contrast, ODI in relation to normal aging is typically linked to alterations in dendritic arborization and/or dendritic complexity (Dickstein et al. 2013; Nazeri et al. 2015; Merluzzi et al. 2016). However, we know of no mechanisms linking unbound iron load with alterations in dendritic arborization and/or dendritic complexity, per se, in older adults. Similarly, alterations in V_{iso} are thought to reflect advanced neurodegenerative change not specific to WM microstructure (Ji et al. 2017; Maillard et al. 2017, 2019). Therefore, our hypotheses focused on relationships with brain iron concentration and ND. Nonetheless, analyses between frontoparietal QSM values, ODI and V_{iso} were conducted for completeness.

Probabilistic tractography

The goal of the tractography analysis was to identify a white-matter network connecting the twelve peak activation fMRI seed ROIs (i.e. a WM-connectivity mask). To this end, probabilistic tractography was conducted in FSL, as described in our previous work (Brown et al. 2015, 2017). Specifically, the following series of procedures were conducted: first, the CUDA/GPU version of BEDPOSTX (BEDPOSTX_GPU) was used to construct per participant maps of the distribution of diffusion parameters at each voxel, from the eddy corrected DWI scans as input (Behrens et al. 2007). The distribution of diffusion parameters was modeled using zeppelins (model 3).

Next, each participant's skull stripped T1 image was aligned/registered to the first b0 image of their eddy-corrected DWI scan using the AFNI function align_epi_anat.py and a local Pearson correlation cost function. The aligned T1 images were then non-linearly warped to MNI152 space (MNI ICBM152 1 mm 6th generation atlas; Grabner et al. 2006) using the AFNI function auto_warp.py. The inverse of the transformation matrices obtained from the previous 2 steps (registration and warping) were then used to inversely warp the 12 seed ROIs from MNI152 space to each participant's DWI data in native space, using the AFNI function 3dNwarpApply and a nearest neighbor cost function. Additionally, the same procedure was used to inversely warp a brainstem mask, created from the Harvard-Oxford Subcortical Atlas (Desikan et al. 2006), which is in MNI152 space, to each participant's eddy corrected DWI data, in native space. This brainstem mask was used to constrain the probabilistic tractography step described below.

Following the steps described above, per participant: distribution of diffusion parameter maps, 12 native-space-warped fMRI seed ROIs and brainstem masks, were used as inputs to the CUDA/GPU version of FSL's PROBTRACKX2 (PROBTRACKX2_GPU) in order to calculate per participant estimates of anatomical connectivity between the fMRI seed ROIs (Behrens et al. 2003, 2007). PROBTRACKX2_GPU was executed using modified Euler streamlining in network mode. Five-thousand streamlines were generated from each voxel within each of the seed ROIs, with a maximum of 2,000 steps per streamline, a step length of 0.5 mm, a minimum streamline length of 20 mm, a curvature threshold of 0.2 (curvature angle could not exceed ~80°), and the default fiber volume threshold of 0.01. To prevent tracking of streamlines in the brainstem, the native-space-warped brainstem mask was used as an exclusion mask. Streamlines were only included in the final output (streamline density map) if all of the following criteria were met: a streamline from 1 seed ROI reached at least 1 of the other seed ROIs, the minimum streamline length requirements were met, the streamline curvature threshold was met (80° or less), the streamline did not exit the brain, loop back on itself, or enter the exclusion brainstem mask.

The output of PROBTRACKX2 is a streamline density map, containing successful streamlines per voxel for each participant. Proportion images were then created by dividing each participant's streamline density map by the sum of all voxels across the seed ROIs. Lastly, each participant's proportion image was divided by their waytotal, the sum of all successfully generated streamlines, in order to account for differences in streamline tracking across participants. Therefore, the waytotal-adjusted proportion images provide a quantitative measure of the proportion/percentage of successful streamlines per voxel. The waytotal-adjusted proportion images were then warped to MNI152 space using the auto_warp.py transformation matrices obtained in previous steps in conjunction with 3dNwarpApply and wsinc5 as the interpolation method. The MNI152 warped, waytotal-adjusted proportion images were then used in a subsequent voxel-wise analysis to obtain a group-level, WM-connectivity mask (see Results, WM-connectivity mask) representing the WM connections between the working memory seed ROIs defined previously.
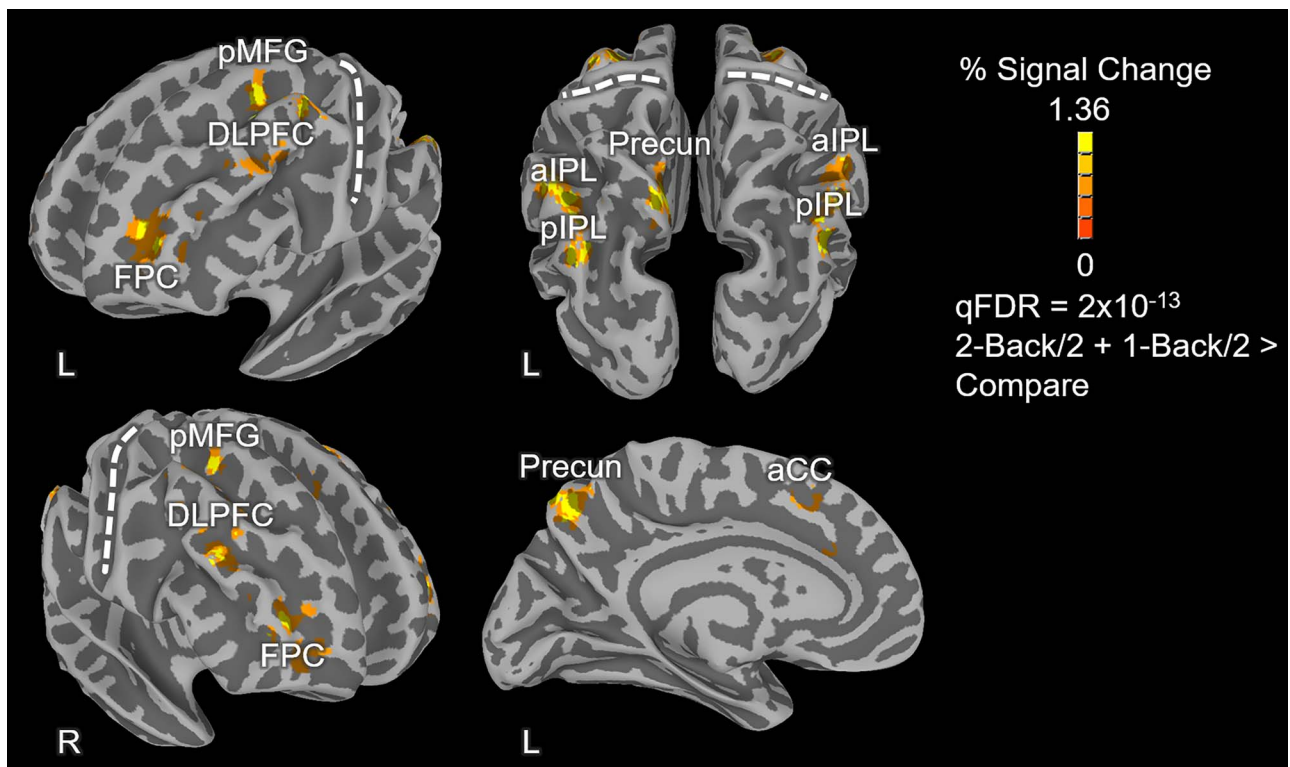
Fig. 1. N-back task activation map. The activation map reflects the voxel-wise functional contrast of 2-back/2 + 1-back/2 > compare. Only positive activations are depicted in the figure in warm (yellow-orange) colors and reflect regions with higher average N-back activity than the control (compare) task. The 3D cortical meshes depicted in the figure were created from the MNI ICBM152, 1 mm, 6th generation atlas using FreeSurfer 6 and were partially inflated to aid identification of activations within sulci. Notes: aCC: anterior cingulate cortex; DLPFC: dorsolateral prefrontal cortex; FPC: frontopolar cortex; pMFG: posterior middle frontal gyrus; Precun: precuneus; aIPL: anterior inferior parietal lobule; pIPL: posterior inferior parietal lobule. The central sulci are marked with dashed white lines to aid visual localization.

Quantitative susceptibility mapping processing

Quantitative susceptibility mapping (QSM) maps were generated using our previously validated software, Ironsmith, which is described in detail elsewhere (Zachariou et al. 2022). In short, Ironsmith uses the MEDI Toolbox (De Rochefort et al. 2010; Liu, Khalidov, et al. 2011; Liu, Liu, et al. 2011; Liu, Liu, et al. 2012) to invert an estimate of the magnetic field that is structurally consistent with anatomy in order to generate a distribution of local magnetic susceptibility values. Ironsmith then uses the local magnetic susceptibility of CSF within the lateral ventricles to scale the QSM maps such that positive values corresponded to local magnetic susceptibility greater than that of CSF and negative values corresponded to local magnetic susceptibility less than that of CSF. CSF within the lateral ventricles was selected as the reference structure for QSM reconstruction because CSF susceptibility is fairly uniform and does not vary with participant demographic variables such as age or gender (Straub et al. 2017).

QSM ROIs

The following procedure was used to create GM-only ROIs from the spherical fMRI seed ROIs. To create these GM-only ROIs, we first inversely warped the spherical fMRI seed ROIs from MNI152 space to each participant's native space using per participant transformation matrices provided by Ironsmith. These transformation matrices are provided by Ironsmith specifically for inversely warping and registering, user-specified ROIs and/or masks from MNI152 space onto the QSM map of each participant in native space. Following the inverse transformation step, all fMRI seed ROIs were resampled/upscaled to the QSM voxel resolution

Table 2. MNI coordinates of activation peaks and corresponding anatomical brain regions identified using the voxel-wise functional contrast of 2-back/2 + 1-back/2 > compare.

Anatomical brain region	Hemi-sphere[a]	MNI coordinates (X, Y, Z)[b]
Anterior cingulate gyrus	L	−6, 24, 43
Dorsolateral prefrontal cortex	L	−44, 29, 33
Dorsolateral prefrontal cortex	R	41, 37, 30
Frontopolar cortex	L	−33, 52, 6
Frontopolar cortex	R	32, 55, 8
Posterior middle frontal gyrus	L	−26, 12, 52
Posterior middle frontal gyrus	R	28, 13, 52
Precuneus	L	−7, −68, 52
Anterior inferior parietal lobule	L	−43, −59, 50
Anterior inferior parietal lobule	R	44, −60, 49
Posterior inferior parietal lobule	L	−34, −77, 42
Posterior inferior parietal lobule	R	42, −72, 37

[a]Hemisphere (L: left; R: right). [b]MNI coordinates, in LPI/SPM order.

(i.e. from 3.0 mm isotropic to 1.2 mm isotropic voxels). Lastly, each upscaled ROI was multiplied (using the AFNI 3dcalc function) by each participant's lobar GM masks provided by Ironsmith in order to eliminate any WM included in the ROIs. The individual GM-only QSM ROIs were then grouped further into larger frontal and parietal lobe ROIs in order to limit the number of multiple comparisons required to test our main hypothesis: that high GM brain iron concentration is associated with reduced WM health within neighboring tracts. The same procedure used by Ironsmith (see section 2.3.9 in Zachariou et al. 2022) was also used here to extract average QSM values from the frontal and parietal lobe
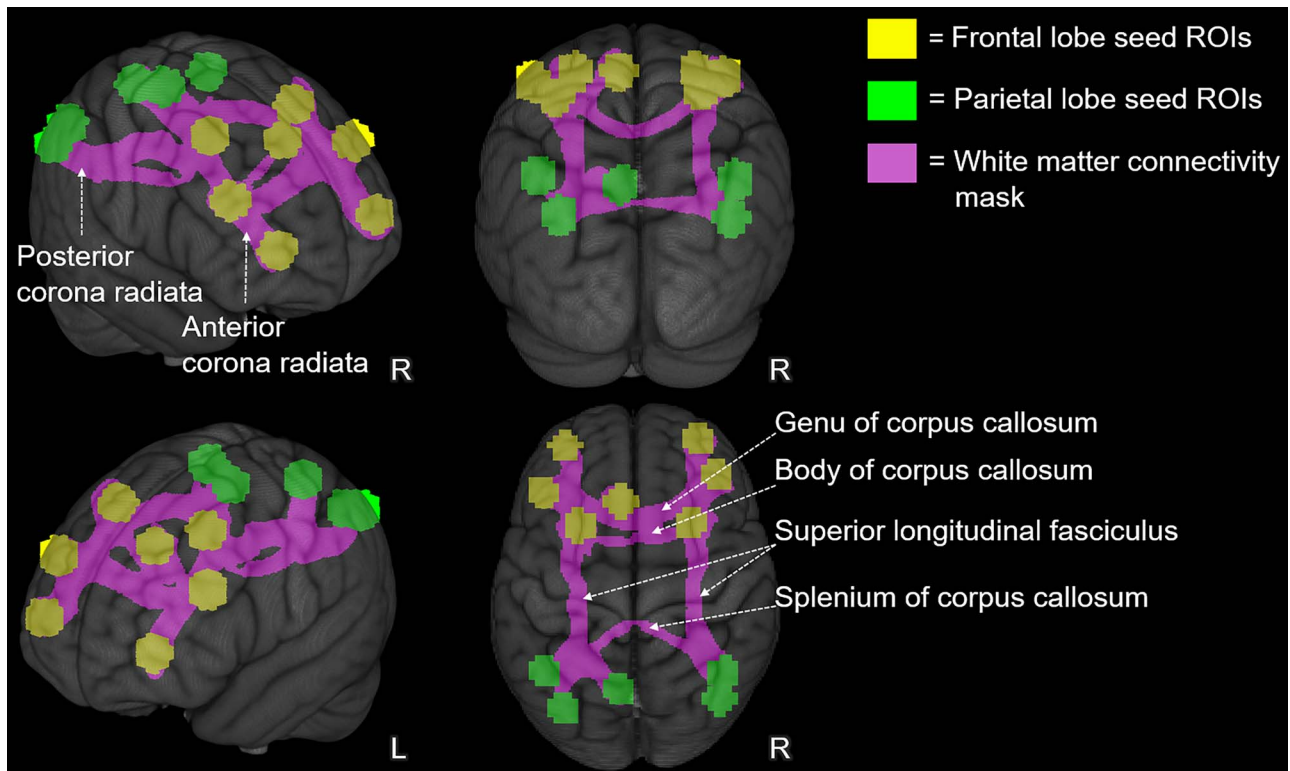
Fig. 2. Group-level, WM-connectivity mask. The figure depicts the group-level, WM tracts/streamlines (in pink), identified using probabilistic tractography, thresholded at the 97th percentile of the average adjusted proportion values. The WM-connectivity mask represents the WM connections between the fMRI working memory seed ROIs. The fMRI seed ROIs are displayed in the figure as yellow (frontal lobe) and green (parietal lobe) spheres. Major WM tracts overlapping with the WM-connectivity mask are labeled. The WM-connectivity map and fMRI seed ROIs are overlaid on the 1 mm, MNI152 template provided with FSL, displayed here as a rendered 3D volume.

ROIs in parts per billion by mm3; ppb/mm3. Namely, only positive QSM values were extracted and QSM values higher than the 97th percentile of all positive QSM values within an ROI were considered outliers and were excluded.

The volume of the frontal and parietal GM ROIs was also calculated per participant using the AFNI function 3dBrickStat. These volumes were then normalized for participant head size using each participant's FreeSurfer-derived estimated intracranial volume (eICV), provided by Ironsmith. The normalized frontal and parietal GM ROI volumes were used in subsequent voxel-wise analyses to control for the potential impact of GM atrophy/neurodegeneration on WM health.

Finally, an additional control ROI was created by summing the bilateral caudate and putamen ROIs provided by Ironsmith (using the AFNI 3dcalc function). QSM values extracted from this basal ganglia ROI and corresponding normalized GM volume were used in a subsequent control analysis to assess the anatomical specificity of our findings. Specifically, we assessed whether QSM values in brain regions distal to fMRI activation peaks would also correlate with ND in the WM-connectivity mask. The basal ganglia was chosen as a control region because it consists of subcortical structures distant to the neocortical fronto-parietal regions showing peak fMRI activation during the working memory task. In addition, the basal ganglia is an appropriate control region because it undergoes significant age-related brain iron accumulation (Hallgren and Sourander 1958; Haacke et al. 2005; Daugherty and Raz 2013).

Group-level, voxel-wise analyses

Group-level analyses were conducted with QSM values from specific ROIs and N-Back task log D-Prime as the independent variables (as mean centered vectors), and voxel-wise ND as the dependent variable, using linear mixed-effects models (3dLME; Chen et al. 2013). These voxel-wise analyses were constrained within the group-level WM-connectivity mask defined previously. The QSM ROIs were the frontal lobe, parietal lobe and basal ganglia, tested in separate analyses. This was required to avoid issues related to collinearity because QSM values extracted from the frontal and parietal lobe ROIs correlated significantly with each other (linear regression: $r^2 = 0.25$, $\beta = 0.526$, $P < 0.0001$, controlling for participant age and gender). Covariates were age (as a mean centered vector), gender (as a categorical, between-subjects variable) and normalized GM volume of corresponding frontal/parietal/basal ganglia ROIs. The resulting statistical maps were thresholded at qFDR < 0.05 using the false discovery rate approach for multiple comparisons correction within the WM connectivity mask (Genovese et al. 2002).

Results
fMRI N-back activation

Whole-brain activations associated with the 1-Back and 2-Back conditions were contrasted with activations during the Compare condition (1-Back/2 + 2-Back/2 > Compare) in order to localize the overall network of brain regions supporting visual working memory. Activation maps were thresholded at qFDR < 2×10^{-13} and all positively active regions (activity stronger for the N-Back than the Compare condition) from this contrast are shown in Fig. 1 and listed in Table 2. The MNI coordinates listed in Table 2 were used as inputs to the Neurosynth database (Yarkoni et al. 2012) and these fMRI ROIs overlapped substantially with core working memory network regions identified in previous studies from a
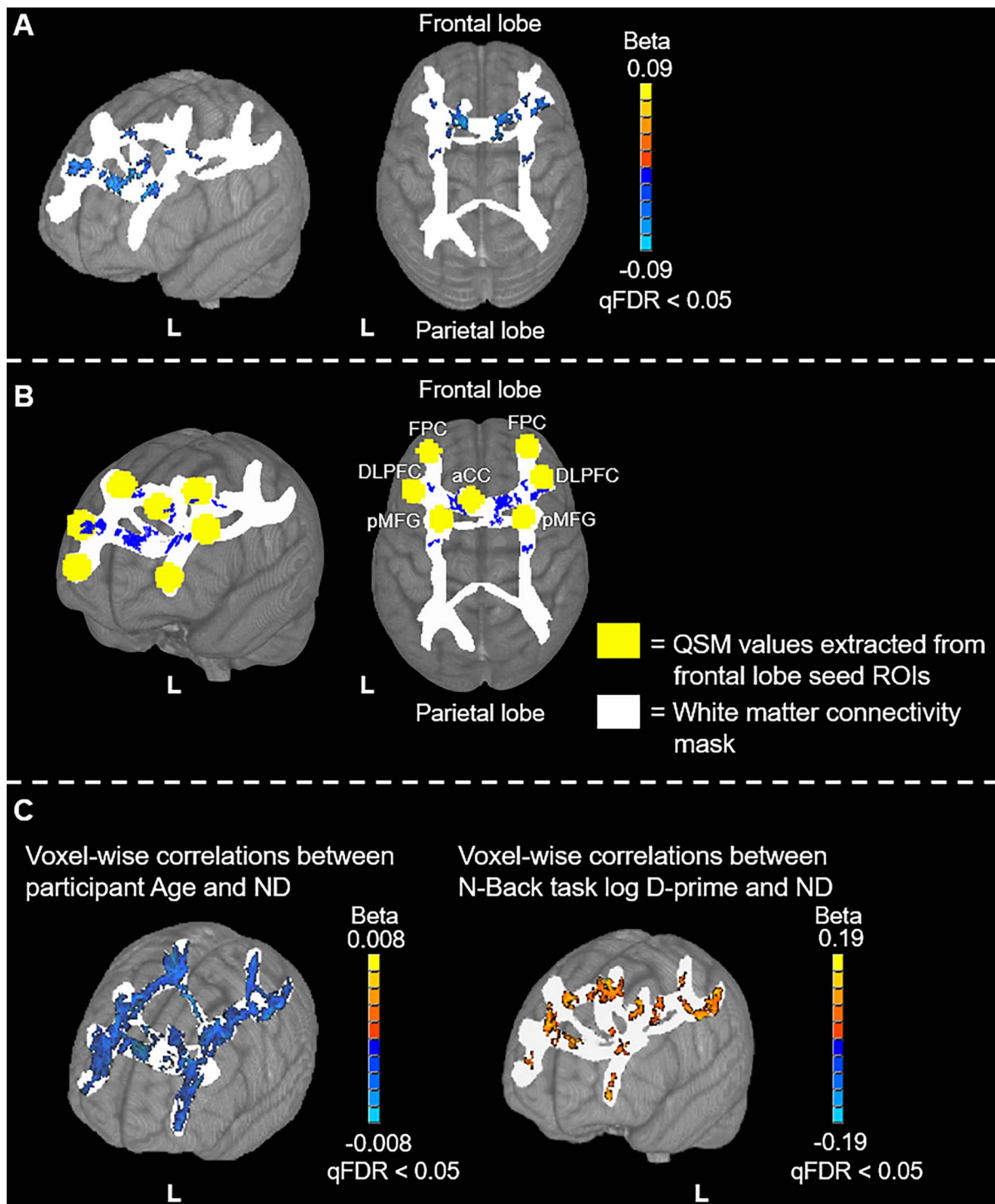
Fig. 3. Voxel-wise results of the frontal lobe QSM vs ND analyses. The frontal lobe seed regions, from which QSM values were extracted for this analysis, are shown in yellow. The WM connectivity mask, in which voxel-wise analyses were performed, is shown in white. Positive correlations are depicted with warm (orange to yellow) colors and negative correlations are depicted with cool (blue to cyan) colors. (A) The correlation with ND results with minimal labeling. (B) A mask of the significantly active voxels in (A) in blue with the frontal lobe seed ROIs depicted as yellow spheres and anatomical labels added. (C) The voxel-wise relationships between age and ND (left) and between N-back task log D-prime and ND (right). Results are overlaid on the 1 mm, MNI152 template provided with FSL, rendered as a 3D volume. Notes: aCC: anterior cingulate cortex; DLPFC: dorsolateral prefrontal cortex; FPC: frontopolar cortex; pMFG: posterior middle frontal gyrus.

meta-analysis sample of 1,334 working memory related articles included in the database.

WM-connectivity mask

To create the WM-connectivity mask, a group level, 1-sample *t*-test (sample compared to zero) was conducted in AFNI, using 3dttest++ on the MNI152 warped, waytotal-adjusted proportion images across participants. The resulting, group-average, waytotal-adjusted, proportion map was then thresholded at the 97th percentile of the average adjusted proportion values. That is, voxels needed to have at least 97% proportion of streamlines passing through them to be included in subsequent analyses.

Table 3. MNI152 coordinates and anatomical labels of voxels showing peak correlation between frontal lobe ROI QSM and ND within the frontoparietal WM-connectivity mask.

WM-tract	Hemi-sphere	MNI coordinates (X, Y, Z)[a]
Anterior corpus callosum	L	8, 6, 24
Anterior corpus callosum	R	−10, 19, 18
DLPFC WM	L	−32, 30, 28
pMFG/DLPFC WM	L	−21, 9, 46
DLPFC WM	R	42, 29, 30
DLPFC WM	R	29, 32, 29
pMFG WM	L	−27, −4, 44
pMFG WM	R	29, −9, 44
Anterior cingulate gyrus WM	L	−15, 21, 44
Anterior cingulate gyrus WM	L	−15, 24, 38
Anterior corona radiata	R	26, 21, 25

Notes: DLPFC: dorsolateral prefrontal cortex; pMFG: posterior middle frontal gyrus; WM: white matter. Hemisphere (L: left; R: right). [a]MNI coordinates, in LPI/SPM order.

Other threshold values (specifically 95% and 90%; Supplementary Fig. S1) were also explored but yielded streamlines connecting to brain regions (in temporal cortex) that were not significantly activated in the fMRI N-Back task (i.e. 1 of the 12 seed ROIs). In contrast, at the 97th percentile threshold, surviving streamlines interconnected only the seed ROIs (Supplementary Fig. S1; 2). After thresholding, the average waytotal-adjusted proportion map was clusterized using AFNI's 3dClustSim function and a minimum cluster size of 100 voxels. Clusterizing was used to remove spurious voxels that survived the 97th percentile threshold but were disconnected from the bulk/main body of the streamlines identified. Lastly, a binary mask (Fig. 2) was created from the surviving voxels and acted as the group-level, WM-connectivity mask in subsequent analyses. The WM-connectivity mask included the splenium, body and genu of the corpus callosum, bilateral portions of the superior longitudinal fasciculus, and bilateral portions of the anterior and posterior corona radiata.

Frontal lobe QSM vs ND

These analyses revealed significant, negative correlations between frontal lobe QSM values and ND in frontal portions of the frontoparietal WM-connectivity mask (Fig. 3A and B). More specifically, the majority of significantly active voxels occurred in WM regions adjacent to the working memory ROIs in frontal cortex. In contrast, no correlations were observed between frontal lobe QSM values and ND in parietal lobe regions of the WM-connectivity mask. The MNI152 coordinates of peak correlation voxels and their corresponding WM tracts are provided in Table 3. Additionally, a positive relationship was observed between N-Back task log D-prime and ND, and a negative relationship between age and ND within the WM-connectivity mask (at qFDR < 0.05). However, in contrast to the anatomically specific relationship between frontal lobe QSM and frontal ND (Fig. 3A and B), N-Back task log D-prime and age correlated with ND throughout the frontoparietal WM-connectivity mask (Fig. 3C). No significant relationships were identified between the normalized frontal lobe ROI GM volumes and ND.

Parietal lobe QSM vs ND

These analyses revealed significant, negative correlations between parietal lobe QSM values and ND in parietal portions of the frontoparietal WM-connectivity mask (Fig. 4). Specifically, this analysis identified 2 bilateral clusters of significant correlations that were anatomically proximal to the working memory ROIs in parietal cortex. No significant correlations were observed between parietal lobe QSM values and ND in frontal lobe regions of the WM-connectivity mask. The MNI152 coordinates of peak correlation voxels and corresponding WM tracts are provided in Table 4. Consistent with results from the frontal lobe analyses described in the previous section, N-Back task log D-prime correlated positively with ND and age correlated negatively with ND throughout the frontoparietal WM-connectivity mask (at qFDR < 0.05; Fig. 3C). Also consistent with the frontal lobe analyses, no significant relationships were identified between the normalized parietal lobe ROI GM volumes and ND.

Control analysis between basal ganglia QSM values and ND

The basal ganglia ROI analysis did not reveal any significant voxels up to an uncorrected P-value of 0.044 (qFDR = 0.998). Thus, neither QSM values extracted from the basal ganglia nor the normalized basal ganglia GM volume correlate significantly with ND within the frontoparietal WM-connectivity mask.

Analyses between frontoparietal QSM values, ODI, and V_{iso}

Voxel-wise analyses between ODI and V_{iso} as dependent variables and fMRI seed ROI QSM values and N-Back task log D-prime as independent variables were conducted for completeness and transparency, with age, gender and normalized GM volume of corresponding frontal/parietal/basal ganglia ROIs used as covariates. These analyses did not reveal significant correlations between frontal/parietal lobe ROI QSM values, ODI, and V_{iso} within the frontoparietal WM-connectivity mask. Consequently, results concerning ODI/V_{iso} are not discussed further.

Mediation analyses

We further tested whether frontal and/or parietal lobe QSM values (in separate analyses) mediated the negative relationship between age and ND we observed in the previous voxel-wise analyses. Due to the anatomical specificity of the voxel-wise associations between QSM and ND, as opposed to the uniform associations between age and ND throughout the frontoparietal WM-connectivity mask, the mediation analyses focused on ND values extracted from those voxels/regions in which significant QSM vs ND associations were observed (the frontal/parietal regions depicted in Figs. 3B and 4B). The mediation analyses were conducted in SPSS using the Andrew F. Hayes PROCESS (version 3.5; model 4) computational tool (Hayes 2019). The mediation results were evaluated at 95% confidence intervals using the default setting of 5,000 bootstrapped samples.

For the frontal lobe analysis, QSM mediated the relationship between age and ND: Indirect effect of age on ND: [Effect = −0.010; SE = 0.0006, bootstrapped confidence interval (LLCI to ULCI) = −0.0023 to −0.0001]. That is, the indirect effect of age on ND, through age-related increases in frontal QSM-based iron concentration, is more likely than the direct effect of age on ND.

For the parietal lobe analyses, QSM did not mediate the relationship between age and ND: Indirect effect of age on ND: [Effect = −0.0009; SE = 0.0006, bootstrapped confidence interval (LLCI to ULCI) = −0.0022 to 0.0001]. That is, the indirect effect of age on ND, through age related increases in parietal lobe QSM-based iron concentration, was not more likely than the direct effect of age on ND.
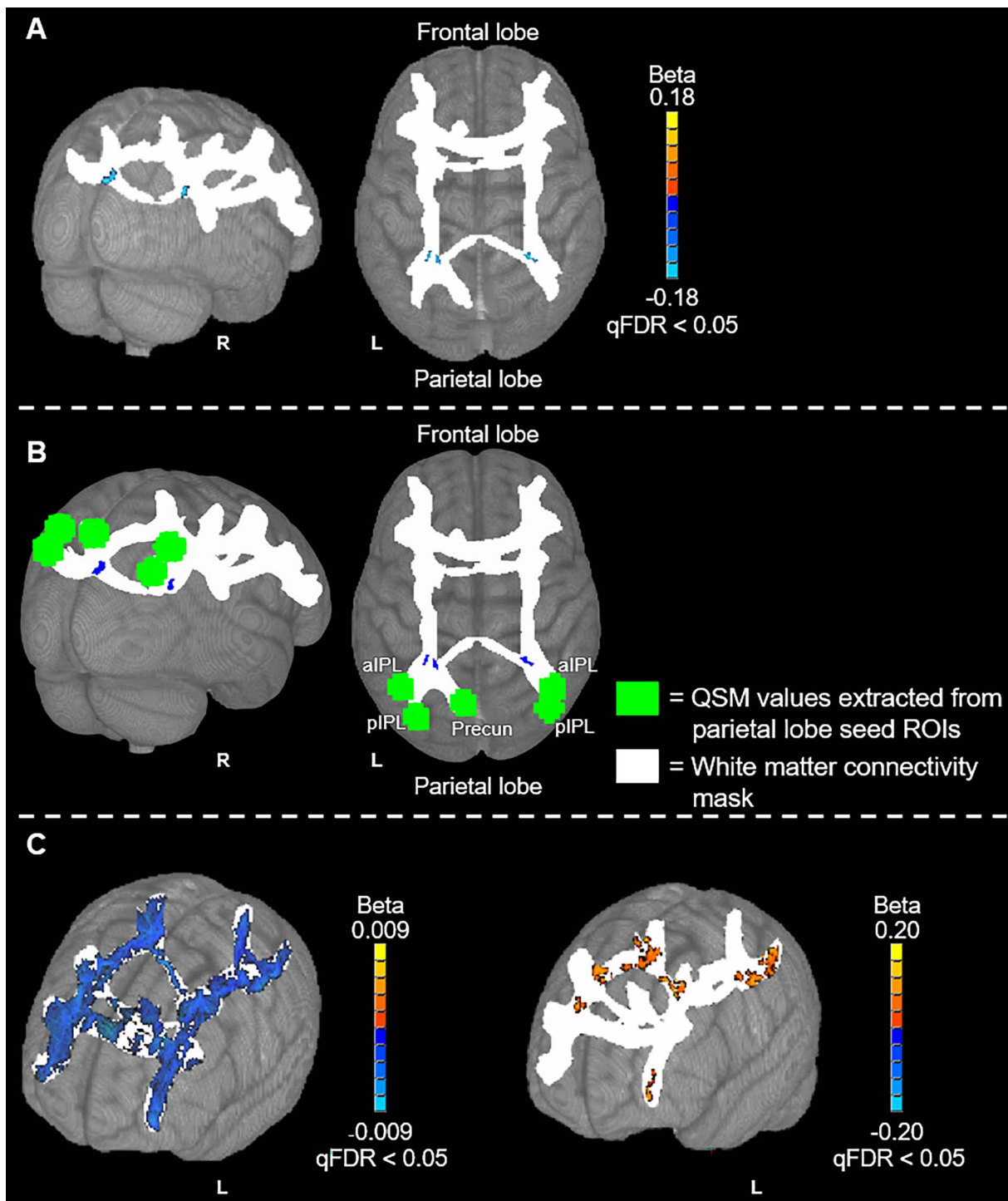
Fig. 4. Voxel-wise results of the parietal lobe QSM vs ND analyses. The parietal lobe QSM seed regions, from which QSM values were extracted for this analysis, are shown in white. The WM-connectivity mask, in which voxel-wise analyses were performed, is shown in white. Positive correlations are depicted with warm (orange to yellow) colors and negative correlations are depicted with cool (blue to cyan) colors. (A) The correlation results with minimal labelling. (B) A mask of the significantly active voxels in (A) in blue with the parietal lobe seed ROIs depicted as green spheres. (C) The voxel-wise relationships between age and ND (left) and between N-back task log D-prime and ND (right). Results are overlaid on the 1 mm, MNI152 template provided with FSL, rendered as a 3D volume. Notes: Precun: precuneus; aIPL: anterior inferior parietal lobule; pIPL: posterior inferior parietal lobule.

Discussion

We investigated associations between cortical iron concentration, WM microstructural properties, age and cognitive performance in healthy older adults. Our results indicated that high ND within WM tracts of a task-relevant working memory brain network supported more accurate working memory performance.

However, high iron load disrupted ND within the same task-relevant WM network. In addition, relationships were anatomically specific such that iron load within frontal and parietal cortical regions were each selectively associated with lower ND within their respective neighboring WM tracts. Our results suggest that age-related increases in brain iron concentration may

Table 4. MNI152 coordinates and anatomical labels of voxels showing peak correlation between parietal lobe QSM and ND within the frontoparietal WM-connectivity mask.

WM-tract	Hemi-sphere[a]	MNI coordinates (X, Y, Z)[b]
Posterior corona radiata	L	−28, −45, 25
Posterior corona radiata	L	−24, −46, 27
Posterior corona radiata	R	28, −47, 23

Notes: WM: white matter. [a]Hemisphere (L: left; R: right). [b]MNI coordinates, in LPI/SPM order.

contribute to disruption of WM tracts supporting cognitive function in normal aging.

The impact of non-heme iron on cognitive brain networks

Our results linking brain iron with WM microstructure build upon recent findings reporting a negative association between brain iron concentration and functional connectivity in older adults (e.g. Salami et al. 2018; Rodrigue et al. 2020; Zachariou et al. 2020). WM connectivity provides the anatomical structure supporting functional connectivity (Sporns et al. 2000; Honey et al. 2009; Betzel et al. 2014) and low ND was associated with poor working memory performance in this study. Consequently, the sum of our current findings and those of prior functional connectivity studies suggest that excess brain iron may interfere with cognitive function by disrupting WM connections between task-relevant brain regions. This iron mediated disruption of WM would be expected to hinder coordinated information processing within task-relevant brain networks (i.e. the functional connectivity of the network).

The impact of non-heme iron on WM microstructure: potential mechanisms

We observed anatomically proximal relationships between cortical iron and ND. Specifically, iron load within frontal cortex was selectively associated with lower ND in neighboring frontal tracts while iron load in parietal cortex was selectively associated with lower ND in parietal lobe tracts. Further, QSM values in the basal ganglia, a region distal to the fMRI activation peaks, was not correlated with ND in the frontoparietal WM-connectivity mask. The anatomical proximity of the QSM/ND relationships we observed is consistent with a view that non-heme iron may accumulate at similar rates in cortical GM and bordering WM. This view is supported by previous histological studies which have shown comparable fixed tissue iron concentrations (mg of iron/Kg fixed tissue) between GM and WM regions (Hametner et al. 2018). As such, while it is not yet possible to directly measure iron concentrations in WM using MRI, QSM-based iron concentration in GM may be a proxy of iron concentration in neighboring WM.

Consequently, it is possible that our results could in part reflect direct effects of brain iron on both GM and neighboring WM, possibly through common underlying mechanisms. A likely common mechanism contributing to deleterious effects of brain iron on both WM and GM relates to iron's propensity for generating free radicals and related oxidative stress (Ward et al. 2014). Oxidative stress results in mitochondrial dysfunction, which can lead to apoptosis (Ward et al. 2014). Specifically, mitochondrial dysfunction related to iron-mediated free radical accumulation reduces the synthesis of high-energy phosphates across brain regions, including cortical regions, subcortical structures, and WM, which promotes age-related tissue damage (Ward et al. 2014; Raz and Daugherty 2018).

Direct effects of brain iron on WM are in-keeping with results showing that antioxidant levels in myelin and oligodendrocytes are relatively low compared to other brain cells, like astrocytes and microglia, making them particularly vulnerable to iron-mediated oxidative stress (Juurlink et al. 1998; Smith et al. 1999). Further, non-heme iron mediated increases in oxidative stress in axons can promote macrophages to attack the myelin sheath directly, leading to WM microstructure damage (Graham et al. 1993). Lastly, iron-mediated mitochondrial dysfunction may also lead to axonal degeneration through the course of impulse conduction. In short, due to the iron mediated energy deficiency, sodium ions (Na +) which enter axons during spiking are not removed. Increased intra-axonal sodium ions can lead to Ca++ accumulation via the inverse operation of the Na +/Ca ++ exchanger, leading to protease-induced axonal degeneration (Stys 2005; Friese et al. 2014; Lassmann and van Horssen 2016).

Finally, our results may also in part reflect indirect, secondary effects of GM degeneration on WM or vice versa. For example, if a soma is damaged as a result of brain-iron mediated oxidative stress, this can result in degeneration of connected axons and their myelin (Damoiseaux et al. 2009; Davis et al. 2009). We did not find direct support for this possibility in the present cross-section study as there was no relationship between normalized GM volume of our ROIs and ND within the WM-connectivity mask. Nevertheless, this possibility should be tested in future longitudinal studies.

The impact of non-heme iron on the relationship between age and WM microstructure

If age-related increases in brain iron contribute to disruption of WM tracts then brain iron may be expected to mediate the relationship between age and WM microstructure. We found partial evidence for this possibility. Consistent with previous results (Cox et al. 2016; Chad et al. 2018; Beck et al. 2021), we found that age was negatively associated with ND throughout the WM tracts of the task-relevant working memory brain network. However, within the frontal lobe, the relationship between age and ND was mediated by brain iron concentration. That is, age-related declines in WM health within task-relevant tracts were partly explained by age-related increases in brain iron. As such, our results provide preliminary evidence suggesting that age-related increases in brain iron concentration, at least in the frontal lobe, may contribute to disruption of WM tracts supporting cognitive function in normal aging.

Strengths

Strengths of our study include the following: 1) robust delineation of brain regions showing strong functional response during a visual N-Back working memory task, consistent with core working memory regions identified in previous studies, (using Neurosynth-based meta-analyses; Yarkoni et al. 2012); 2) Probabilistic tractography-based delineation of WM tracts interconnecting these regions, identifying a network of tracts known to be associated with working memory and other executive function tasks (Kennedy and Raz 2009; Madden, Bennett, & Song 2009; Madden, Spaniol, et al. 2009; Zahr et al. 2009; Gold et al. 2010); 3) Use of QSM for assessing brain iron concentration. QSM overcomes several limitations of prior MRI-based methods for evaluating brain iron load, including orientation dependence and non-local effects (Shmueli et al. 2009; Liu, Liu, et al. 2012); 4) Evaluation of WM health using NODDI, which is a more

sensitive method, and more closely linked to biology, than more traditional DTI-based metrics such as FA, mean, axial, and radial diffusivity (Jespersen et al. 2010; Sepehrband et al. 2015; By et al. 2017; Schneider et al. 2017; Wang et al. 2019); 5) inclusion of normalized GM volume of the fMRI seed ROIs as a covariate in all analyses models, in order to assess the impact of neurodegeneration, (within the limits this can be measured using GM volume) on the findings, which was negligible.

Limitations

It should be noted that brain iron may influence the measurement of diffusion based metrics in GM regions (specifically deep GM, such as within the basal ganglia), where diffusion weighted imaging signal is low, water diffusion is isotropic and iron concentration is high (e.g. Rulseh et al. 2013 ; Xu et al. 2015). Specifically, GM iron has been reported to enhance DTI-based metrics such as fractional anisotropy (FA) in deep GM structures (Rulseh et al. 2013; Xu et al. 2015). In the present study we focused exclusively on diffusion measures within WM regions. Therefore, the artifact associated with deep GM structures in question is likely not directly relevant to our results. Nevertheless, it is important to remain aware of this issue as the field of QSM-diffusion research evolves. For example, in the current study, we found that higher brain iron concentration in GM was associated with lower ND, a metric that depends on the same underlying diffusion information as FA (the directionality of water diffusion). Thus, if we assume that brain iron may artifactually increase not just FA/ND in deep GM, but also increase these metrics in WM regions, then QSM-diffusion studies may under-estimate the negative influence of brain iron on WM microstructure.

Further, it should be noted that QSM is not a direct measure of iron concentration and can be affected to a lesser extent by the presence of other metals (Wang et al. 2017). In addition, this is a cross-sectional study and causal inferences cannot be made between QSM-based iron concentration and WM microstructure health. As such, we are unable to rule out the possibility that brain iron accumulation results from demyelination rather than being caused by it (Bjartmar and Trapp 2001). For example, axonal demyelination can trigger neurodegenerative processes and lead to intracellular non-heme iron accumulation in corresponding neuronal bodies (Williams et al. 2012). Future longitudinal studies will be required to determine if brain iron predicts demyelination or vice versa.

Conclusion

Our results suggest that non-heme brain iron may contribute to the disruption of WM connectivity in healthy older adults. Specifically, our results indicate that cortical non-heme brain iron concentration load is associated with low ND within a WM network supporting working memory in cognitively normal older adults. Future research should investigate interventions that may slow brain iron accumulation in aging.

Acknowledgments

Supplementary material

Supplementary material is available at *Cerebral Cortex* online.

Authors' contributions

Valentinos Zachariou: conceptualization, methodology, software, formal analysis, data curation, writing—original draft, writing—review & editing, visualization; Christopher E. Bauer: methodology, formal analysis, data curation, investigation, writing—review & editing; Colleen Pappas: writing—review & editing; and Brian T. Gold: conceptualization, methodology, writing—review & editing, supervision, project administration, funding acquisition.

References

Acosta-Cabronero J, Machts J, Schreiber S, Abdulla S, Kollewe K, Petri S, Spotorno N, Kaufmann J, Heinze H-J, Dengler R, et al. Quantitative susceptibility MRI to detect brain iron in amyotrophic lateral sclerosis. *Radiology*. 2018:289(1):195–203.

Andersson JLR, Sotiropoulos SN. An integrated approach to correction for off-resonance effects and subject movement in diffusion MR imaging. *NeuroImage*. 2016:125:1063–1078.

Andersson JLR, Skare S, Ashburner J. How to correct susceptibility distortions in spin-echo echo-planar images: application to diffusion tensor imaging. *NeuroImage*. 2003:20(2):870–888.

Bartzokis G, Lu PH, Tingus K, Peters DG, Amar CP, Tishler TA, Finn JP, Villablanca P, Altshuler LL, Mintz J, et al. Gender and iron genes may modify associations between brain iron and memory in healthy aging. *Neuropsychopharmacology*. 2011:36(7):1375–1384.

Bastiani M, Cottaar M, Fitzgibbon SP, Suri S, Alfaro-Almagro F, Sotiropoulos SN, Jbabdi S, Andersson JLR. Automated quality control for within and between studies diffusion MRI data using a non-parametric framework for movement and distortion correction. *NeuroImage*. 2019:184:801–812.

Beck D, de Lange AM, Maximov II, Richard G, Andreassen OA, Nordvik JE, Westlye LT. White matter microstructure across the adult lifespan: a mixed longitudinal and cross-sectional study using advanced diffusion models and brain-age prediction. *NeuroImage*. 2021:224:117441.

Behrens TEJ, Woolrich MW, Jenkinson M, Johansen-Berg H, Nunes RG, Clare S, Matthews PM, Brady JM, Smith SM. Characterization and propagation of uncertainty in diffusion-weighted MR imaging. *Magn Reson Med*. 2003:50(5):1077–1088.

Behrens TEJ, Berg HJ, Jbabdi S, Rushworth MFS, Woolrich MW. Probabilistic diffusion tractography with multiple fibre orientations: what can we gain? *NeuroImage*. 2007:34(1):144–155.

Bergsland N, Tavazzi E, Laganà MM, Baglio F, Cecconi P, Viotti S, Zivadinov R, Baselli G, Rovaris M. White matter tract injury is associated with deep gray matter iron deposition in multiple sclerosis. *J Neuroimaging*. 2017:27(1):107–113.

Besser L, Kukull W, Knopman DS, Chui H, Galasko D, Weintraub S, Jicha G, Carlsson C, Burns J, Quinn J, et al. Version 3 of the national Alzheimer's coordinating center's uniform data set. *Alzheimer Dis Assoc Disord*. 2018:32(4):351–358.

Betzel RF, Byrge L, He Y, Goñi J, Zuo XN, Sporns O. Changes in structural and functional connectivity among resting-state networks across the human lifespan. *NeuroImage*. 2014:102:345–357.

Bjartmar C, Trapp BD. Axonal and neuronal degeneration in multiple sclerosis: mechanisms and functional consequences. *Curr Opin Neurol*. 2001:14(3):271–278.

Brown CA, Hakun JG, Zhu Z, Johnson NF, Gold BT. White matter microstructure contributes to age-related declines in task-induced deactivation of the default mode network. *Front Aging Neurosci*. 2015:7:1–10.

Brown CA, Johnson NF, Anderson-Mooney AJ, Jicha GA, Shaw LM, Trojanowski JQ, Van Eldik LJ, Schmitt FA, Smith CD, Gold BT. Development, validation and application of a new fornix template for studies of aging and preclinical Alzheimer's disease. *NeuroImage Clin*. 2017:13:106–115.

Butterfield DA, Halliwell B. Oxidative stress, dysfunctional glucose metabolism and Alzheimer disease. *Nat Rev Neurosci*. 2019:20(3):148–160.

By S, Xu J, Box BA, Bagnato FR, Smith SA. Application and evaluation of NODDI in the cervical spinal cord of multiple sclerosis patients. *NeuroImage Clin*. 2017:15:333–342.

Chad JA, Pasternak O, Salat DH, Chen JJ. Re-examining age-related differences in white matter microstructure with free-water corrected diffusion tensor imaging. *Neurobiol Aging*. 2018:71:161–170.

Chakravarti B, Chakravarti DN. Oxidative modification of proteins: age-related changes. *Gerontology*. 2007:53(3):128–139.

Chen G, Saad ZS, Britton JC, Pine DS, Cox RW. Linear mixed-effects modeling approach to FMRI group analysis. *NeuroImage*. 2013:73:176–190.

Cox RW. AFNI: software for analysis and visualization of functional magnetic resonance neuroimages. *Comput Biomed Res*. 1996:29(3):162–173.

Cox SR, Ritchie SJ, Tucker-Drob EM, Liewald DC, Hagenaars SP, Davies G, Wardlaw JM, Gale CR, Bastin ME, Deary IJ. Ageing and brain white matter structure in 3,513 UK biobank participants. *Nat Commun*. 2016:7(1):1–13.

Dale AM, Fischl B, Sereno MI. Cortical surface-based analysis: I. segmentation and surface reconstruction. *NeuroImage*. 1999:9(2):179–194.

Damoiseaux JS, Smith SM, Witter MP, Sanz-Arigita EJ, Barkhof F, Scheltens P, Stam CJ, Zarei M, Rombouts SARB. White matter tract integrity in aging and Alzheimer's disease. *Hum Brain Mapp*. 2009:30(4):1051–1059.

Darki F, Nemmi F, Möller A, Sitnikov R, Klingberg T. Quantitative susceptibility mapping of striatum in children and adults, and its association with working memory performance. *NeuroImage*. 2016:136:208–214.

Daugherty A, Raz N. Age-related differences in iron content of subcortical nuclei observed in vivo: a meta-analysis. *NeuroImage*. 2013:70:113–121.

Daugherty AM, Raz N. Accumulation of iron in the putamen predicts its shrinkage in healthy older adults: a multi-occasion longitudinal study. *NeuroImage*. 2016:128:11–20.

Daugherty AM, Haacke EM, Raz N. Striatal iron content predicts its shrinkage and changes in verbal working memory after two years in healthy adults. *J Neurosci*. 2015:35(17):6731–6743.

Davis SW, Dennis NA, Buchler NG, White LE, Madden DJ, Cabeza R. Assessing the effects of age on long white matter tracts using diffusion tensor tractography. *NeuroImage*. 2009:46(2):530–541.

De Rochefort L, Liu T, Kressler B, Liu J, Spincemaille P, Lebon V, Wu J, Wang Y. Quantitative susceptibility map reconstruction from MR phase data using Bayesian regularization: validation and application to brain imaging. *Magn Reson Med*. 2010:63(1):194–206.

Desikan RS, Ségonne F, Fischl B, Quinn BT, Dickerson BC, Blacker D, Buckner RL, Dale AM, Maguire RP, Hyman BT, et al. An automated labeling system for subdividing the human cerebral cortex on MRI scans into gyral based regions of interest. *NeuroImage*. 2006:31(3):968–980.

Dickstein DL, Weaver CM, Luebke JI, Hof PR. Dendritic spine changes associated with normal aging. *Neuroscience*. 2013:251:21–32.

Friese MA, Schattling B, Fugger L. Mechanisms of neurodegeneration and axonal dysfunction in multiple sclerosis. *Nat Rev Neurol*. 2014:10(4):225–238.

Genovese CR, Lazar NA, Nichols T. Thresholding of statistical maps in functional neuroimaging using the false discovery rate. *NeuroImage*. 2002:15(4):870–878.

Gold BT, Powell DK, Xuan L, Jicha GA, Smith CD. Age-related slowing of task switching is associated with decreased integrity of frontoparietal white matter. *Neurobiol Aging*. 2010:31(3):512–522.

Grabner G, Janke AL, Budge MM, Smith D, Pruessner J, Collins DL. 2006. Symmetric atlasing and model based segmentation: an application to the hippocampus in older adults. In: *Lecture Notes in Computer Science (including subseries Lecture Notes in Artificial Intelligence and Lecture Notes in Bioinformatics)*. Springer Verlag. p. 58–66.

Graham A, Hogg N, Kalyanaraman B, O'Leary V, Darley-Usmar V, Moncada S. Peroxynitrite modification of low-density lipoprotein leads to recognition by the macrophage scavenger receptor. *FEBS Lett*. 1993:330(2):181–185.

Haacke EM, Cheng NYC, House MJ, Liu Q, Neelavalli J, Ogg RJ, Khan A, Ayaz M, Kirsch W, Obenaus A. Imaging iron stores in the brain using magnetic resonance imaging. *Magn Reson Imaging*. 2005:23(1):1–25.

Hallgren B, Sourander P. The effect of age on the non-haemin iron in the human brain. *J Neurochem*. 1958:3(1):41–51.

Hametner S, Endmayr V, Deistung A, Palmrich P, Prihoda M, Haimburger E, Menard C, Feng X, Haider T, Leisser M, et al. The influence of brain iron and myelin on magnetic susceptibility and effective transverse relaxation - a biochemical and histological validation study. *NeuroImage*. 2018:179:117–133.

Hayes AF. *Introduction to mediation, moderation, and conditional process analysis*. Guilford Press; 2019

Hentze MW, Muckenthaler MU, Andrews NC. Balancing acts. *Cell*. 2004:117(3):285–297.

Honey CJ, Sporns O, Cammoun L, Gigandet X, Thiran JP, Meuli R, Hagmann P. Predicting human resting-state functional connectivity from structural connectivity. *Proc Natl Acad Sci U S A*. 2009:106(6):2035–2040.

Hong H, Wang S, Yu X, Jiaerken Y, Guan X, Zeng Q, Yin X, Zhang R, Zhang Y, Zhu Z, et al. White matter tract injury by MRI in CADASIL patients is associated with iron accumulation. *J Magn Reson Imaging*. 2022. https://doi.org/10.1002/jmri.28301

Jenkinson M, Beckmann CF, Behrens TEJ, Woolrich MW, Smith SM. FSL. *NeuroImage*. 2012:62(2):782–790.

Jespersen SN, Bjarkam CR, Nyengaard JR, Chakravarty MM, Hansen B, Vosegaard T, Østergaard L, Yablonskiy D, Chr N, Vestergaard-poulsen P. Neurite density from magnetic resonance diffusion measurements at ultrahigh field: comparison with light microscopy and electron microscopy. *NeuroImage*. 2010:49(1):205–216.

Ji F, Pasternak O, Liu S, Loke YM, Choo BL, Hilal S, Xu X, Ikram MK, Venketasubramanian N, Chen CLH, et al. Distinct white matter microstructural abnormalities and extracellular water increases relate to cognitive impairment in Alzheimer's disease with and without cerebrovascular disease. *Alzheimers Res Ther*. 2017:9(1):1–10.

Jokinen H, Schmidt R, Ropele S, Fazekas F, Gouw AA, Barkhof F, Scheltens P, Madureira S, Verdelho A, Ferro JM, et al. Diffusion

changes predict cognitive and functional outcome: the LADIS study. *Ann Neurol*. 2013:73(5):576–583.

Juurlink BHJ, Thorburne SK, Hertz L. Peroxide-scavenging deficit underlies oligodendrocyte susceptibility to oxidative stress. *Glia*. 1998:22(4):371–378.

Ke Y, Qian ZM. Brain iron metabolism: neurobiology and neurochemistry. *Prog Neurobiol*. 2007:83(3):149–173.

Kennedy KM, Raz N. Aging white matter and cognition: differential effects of regional variations in diffusion properties on memory, executive functions, and speed. *Neuropsychologia*. 2009:47:916–927.

Kim HG, Park S, Rhee HY, Lee KM, Ryu CW, Rhee SJ, Lee SY, Wang Y, Jahng GH. Quantitative susceptibility mapping to evaluate the early stage of Alzheimer's disease. *NeuroImage Clin*. 2017:16:429–438.

Langkammer C, Schweser F, Krebs N, Deistung A, Goessler W, Scheurer E, Sommer K, Reishofer G, Yen K, Fazekas F, et al. Quantitative susceptibility mapping (QSM) as a means to measure brain iron? A post mortem validation study. *NeuroImage*. 2012:62(3):1593–1599.

Lassmann H, van Horssen J. Oxidative stress and its impact on neurons and glia in multiple sclerosis lesions. *Biochim Biophys Acta - Mol Basis Dis*. 2016:1862(3):506–510.

Lauffer RB. *Introduction iron, aging, and human disease: historical background and new hypotheses*. 1st ed. CRC Press; 1992

Liu T, Khalidov I, de Rochefort L, Spincemaille P, Liu J, Tsiouris AJ, Wang Y. A novel background field removal method for MRI using projection onto dipole fields (PDF). *NMR Biomed*. 2011:24(9):1129–1136.

Liu T, Liu J, de Rochefort L, Spincemaille P, Khalidov I, Ledoux JR, Wang Y. Morphology enabled dipole inversion (MEDI) from a single-angle acquisition: comparison with COSMOS in human brain imaging. *Magn Reson Med*. 2011:66(3):777–783.

Liu J, Liu T, de Rochefort L, Ledoux J, Khalidov I, Chen W, Tsiouris AJ, Wisnieff C, Spincemaille P, Prince MR, et al. Morphology enabled dipole inversion for quantitative susceptibility mapping using structural consistency between the magnitude image and the susceptibility map. *NeuroImage*. 2012:59(3):2560–2568.

Liu T, Surapaneni K, Lou M, Cheng L, Spincemaille P, Wang Y. Cerebral microbleeds: burden assessment by using quantitative susceptibility mapping. *Radiology*. 2012:262(1):269–278.

Madden DJ, Bennett IJ, Song AW. Cerebral white matter integrity and cognitive aging: contributions from diffusion tensor imaging. *Neuropsychol Rev*. 2009:19(4):415–435.

Madden DJ, Spaniol J, Costello MC, Bucur B, White LE, Cabeza R, Davis SW, Dennis NA, Provenzale JM, Huettel SA. Cerebral white matter integrity mediates adult age differences in cognitive performance. *J Cogn Neurosci*. 2009:21(2):289–302.

Maillard P, Mitchell GF, Himali JJ, Beiser A, Fletcher E, Tsao CW, Pase MP, Satizabal CL, Vasan RS, Seshadri S, et al. Aortic stiffness, increased White matter free water, and altered microstructural integrity: a continuum of injury. *Stroke*. 2017:48(6):1567–1573.

Maillard P, Fletcher E, Singh B, Martinez O, Johnson DK, Olichney JM, Farias ST, Decarli C. Cerebral white matter free water: a sensitive biomarker of cognition and function. *Neurology*. 2019:92(19):E2221–E2231.

Merluzzi AP, Dean DC, Adluru N, Suryawanshi GS, Okonkwo OC, Oh JM, Hermann BP, Sager MA, Asthana S, Zhang H, et al. Age-dependent differences in brain tissue microstructure assessed with neurite orientation dispersion and density imaging. *Neurobiol Aging*. 2016:43:79–88.

Mills E, Dong X-P, Wang F, Xu H. Mechanisms of brain iron transport: insight into neurodegeneration and CNS disorders. *Future Med Chem*. 2010:2(1):51–64.

Moos T, Nielsen TR, Skjørringe T, Morgan EH. Iron trafficking inside the brain. *J Neurochem*. 2007:103(5):1730–1740.

Morris JC, Weintraub S, Chui HC, Cummings J, DeCarli C, Ferris S, Foster NL, Galasko D, Graff-Radford N, Peskind ER, et al. The uniform data set (UDS): clinical and cognitive variables and descriptive data from Alzheimer disease Centers. *Alzheimer Dis Assoc Disord*. 2006:20(4):210–216.

Nasreddine ZS, Phillips NA, Bédirian V, Charbonneau S, Whitehead V, Collin I, Cummings JL, Chertkow H. The Montreal cognitive assessment, MoCA: a brief screening tool for mild cognitive impairment. *J Am Geriatr Soc*. 2005:53(4):695–699.

Nazeri A, Chakravart M, Rotenberg DJ, Rajji TK, Rathi X, Michailovich OV, Voineskos AN. Functional consequences of neurite orientation dispersion and density in humans across the adult lifespan. *J Neurosci*. 2015:35:1753–1762.

Rahmanzadeh R, Lu P, Barakovic M, Weigel M, Maggi P, Nguyen TD, Schiavi S, Daducci A, la Rosa F, Schaedelin S, et al. Myelin and axon pathology in multiple sclerosis assessed by myelin water and multi-shell diffusion imaging. *Brain*. 2021:144(6):1684–1696.

Raz N, Daugherty AM. Pathways to brain aging and their modifiers: free-radical-induced energetic and neural decline in senescence (FRIENDS) model - a mini-review. *Gerontology*. 2018:64(1):49–57.

Raz E, Branson B, Jensen JH, Bester M, Babb JS, Herbert J, Grossman RI, Inglese M. Relationship between iron accumulation and white matter injury in multiple sclerosis: a case-control study. *J Neurol*. 2015:262(2):402–409.

Rodrigue KM, Daugherty AM, Foster CM, Kennedy KM. Striatal iron content is linked to reduced fronto-striatal brain function under working memory load. *NeuroImage*. 2020:210:116544.

Rulseh AM, Keller J, Tintěra J, Kožíšek M, Vymazal J. Chasing shadows: what determines DTI metrics in gray matter regions? An in vitro and in vivo study. *J Magn Reson Imaging*. 2013:38(5):1103–1110.

Salami A, Avelar-Pereira B, Garzón B, Sitnikov R, Kalpouzos G. Functional coherence of striatal resting-state networks is modulated by striatal iron content. *NeuroImage*. 2018:183:495–503.

Schneider T, Brownlee W, Zhang H, Ciccarelli O, Miller DH, Wheeler-Kingshott CG. Sensitivity of multi-shell NODDI to multiple sclerosis white matter changes: a pilot study. *Funct Neurol*. 2017:32(2):97–101.

Schmitt FA, Nelson PT, Abner E, Scheff S, Jicha GA, Smith C, Cooper G, Mendiondo M, Danner DD, Van Eldik LJ, et al. University of Kentucky Sanders-Brown healthy brain aging volunteers: donor characteristics, procedures and neuropathology. *Curr Alzheimer Res*. 2013:9:724–733.

Sepehrband F, Clark KA, Ullmann JFP, Kurniawan ND, Leanage G, Reutens DC, Yang Z. Brain tissue compartment density estimated using diffusion-weighted MRI yields tissue parameters consistent with histology. *Hum Brain Mapp*. 2015:36(9):3687–3702.

Shmueli K, De Zwart JA, Van Gelderen P, Li TQ, Dodd SJ, Duyn JH. Magnetic susceptibility mapping of brain tissue in vivo using MRI phase data. *Magn Reson Med*. 2009:62(6):1510–1522.

Smith SM. Fast robust automated brain extraction. *Hum Brain Mapp*. 2002:17(3):143–155.

Smith KJ, Kapoor R, Felts PA. Demyelination: the role of reactive oxygen and nitrogen species. *Brain Pathol*. 1999:9(1):69–92.

Smith SM, Jenkinson M, Woolrich MW, Beckmann CF, Behrens TEJ, Johansen-Berg H, Bannister PR, De Luca M, Drobnjak I, Flitney DE, et al. Advances in functional and structural MR image analysis and implementation as FSL. *NeuroImage*. 2004:23:S208–S219.

Sporns O, Tononi G, Edelman GM. Theoretical neuroanatomy: relating anatomical and functional connectivity in graphs and cortical connection matrices. *Cereb Cortex*. 2000:10(2):127–141.

Stanislaw H, Todorov N. Calculation of signal detection theory measures. *Behav Res Methods Instrum Comput*. 1999:31(1):137–149.

Straub S, Schneider TM, Emmerich J, Freitag MT, Ziener CH, Schlemmer HP, Ladd ME, Laun FB. Suitable reference tissues for quantitative susceptibility mapping of the brain. *Magn Reson Med*. 2017:78(1):204–214.

Stys PK. General mechanisms of axonal damage and its prevention. *J Neurol Sci*. 2005:233(1-2):3–13.

Sullivan EV, Adalsteinsson E, Rohlfing T, Pfefferbaum A. Relevance of iron deposition in deep Gray matter brain structures to cognitive and motor performance in healthy elderly men and women: exploratory findings. *Brain Imaging Behav*. 2009:3(2):167–175.

Sun H, Walsh AJ, Lebel RM, Blevins G, Catz I, Lu J-Q, Johnson ES, Emery DJ, Warren KG, Wilman AH. Validation of quantitative susceptibility mapping with Perls' iron staining for subcortical gray matter. *NeuroImage*. 2015:105:486–492.

Todorich B, Pasquini JM, Garcia CI, Paez PM, Connor JR. Oligodendrocytes and myelination: the role of iron. *Glia*. 2009:57(5):467–478.

van Bergen JMG, Li X, Quevenco FC, Gietl AF, Treyer V, Meyer R, Buck A, Kaufmann PA, Nitsch RM, van Zijl PCM, et al. Simultaneous quantitative susceptibility mapping and flutemetamol-PET suggests local correlation of iron and β-amyloid as an indicator of cognitive performance at high age. *NeuroImage*. 2018:174: 308–316.

van der Kouwe AJW, Benner T, Salat DH, Fischl B. Brain morphometry with multiecho MPRAGE. *NeuroImage*. 2008:40:559–569.

Wang Y, Spincemaille P, Liu Z, Dimov A, Deh K, Li J, Zhang Y, Yao Y, Gillen KM, Wilman AH, et al. Clinical quantitative susceptibility mapping (QSM): biometal imaging and its emerging roles in patient care. *J Magn Reson Imaging*. 2017:46(4):951–971.

Wang N, Zhang J, Cofer G, Qi Y, Anderson RJ, White LE, Allan Johnson G. Neurite orientation dispersion and density imaging of mouse brain microstructure. *Brain Struct Funct*. 2019:224(5): 1797–1813.

Ward RJ, Zucca FA, Duyn JH, Crichton RR, Zecca L. The role of iron in brain ageing and neurodegenerative disorders. *Lancet Neurol*. 2014:13(10):1045–1060.

Wayne Martin WR, Ye FQ, Allen PS. Increasing striatal iron content associated with normal aging. *Mov Disord*. 1998:13(2): 281–286.

Williams R, Buchheit CL, Berman NEJ, Levine SM. Pathogenic implications of iron accumulation in multiple sclerosis. *J Neurochem*. 2012:120(1):7–25.

Xu X, Wang Q, Zhong J, Zhang M. Iron deposition influences the measurement of water diffusion tensor in the human brain: a combined analysis of diffusion and iron-induced phase changes. *Neuroradiology*. 2015:57(11):1169–1178.

Yarkoni T, Poldrack RA, Nichols TE, van Essen DC, Wager TD. Large-scale automated synthesis of human functional neuroimaging data. *Nat Methods*. 2012:8(8):665–670.

Zachariou V, Bauer CE, Seago ER, Raslau FD, Powell DK, Gold BT. Cortical iron disrupts functional connectivity networks supporting working memory performance in older adults. *NeuroImage*. 2020:223:117309.

Zachariou V, Bauer CE, Seago ER, Panayiotou G, Hall ED, Butterfield DA, Gold BT. Healthy dietary intake moderates the effects of age on brain iron concentration and working memory performance. *Neurobiol Aging*. 2021:106:183–196.

Zachariou V, Bauer CE, Powell DK, Gold BT. Ironsmith: an automated pipeline for QSM-based data analyses. *NeuroImage*. 2022:249:118835.

Zahr NM, Rohlfing T, Pfefferbaum A, Sullivan EV. Problem solving, working memory, and motor correlates of association and commissural fiber bundles in normal aging: a quantitative fiber tracking study. *NeuroImage*. 2009:44(3):1050–1062.

Zecca L, Stroppolo A, Gatti A, Tampellini D, Toscani M, Gallorini M, Giaveri G, Arosio P, Santambrogio P, Fariello RG, et al. The role of iron and copper molecules in the neuronal vulnerability of locus coeruleus and substantia nigra during aging. *Proc Natl Acad Sci U S A*. 2004:101(26):9843–9848.

Zecca L, Youdim MBH, Riederer P, Connor JR, Crichton RR. Iron, brain ageing and neurodegenerative disorders. *Nat Rev Neurosci*. 2004:5(11):863–873.

Zhang H, Schneider T, Wheeler-Kingshott CA, Alexander DC. NODDI: practical in vivo neurite orientation dispersion and density imaging of the human brain. *NeuroImage*. 2012:61(4):1000–1016.

Zivadinov R, Tavazzi E, Bergsland N, Hagemeier J, Lin F, Dwyer MG, Carl E, Kolb C, Hojnacki D, Ramasamy D, et al. Brain iron at quantitative MRI is associated with disability in multiple sclerosis. *Radiology*. 2018:289(2):487–496.